We do not explicitly consider heterogeneity in sexual activity, although the results are robust to consideration of contact networks and stratification of the population (see Supplementary Methods).

The hazard of infection for susceptible individuals in the ith population is

$$\lambda_i = (1-\varepsilon)\beta_i y_i + \varepsilon\beta_i \bar{y} \quad (1)$$

where ε is the fraction of contacts that are global, β_i the transmission parameter for population i, and $\bar{y}$ is the prevalence among global contacts, which is simply the average prevalence over the n populations of the metapopulation weighted by the transmission parameter β_i to ensure numbers of contacts between populations balance ($\bar{y} = \sum_n Y_i\beta_i / \sum_n N_i\beta_i$). This type of representation of coupling between populations has been shown to be a good approximation to more explicit mechanistic models of migration, where individuals spend periods outside their 'home' city[21,22].

The stochastic version of this model can give sustained oscillations in prevalence and incidence due to continued perturbation of the system by random events[16]. In the case that $\varepsilon = 0$, prevalence in each population oscillates with period

$$T = 2\pi / \sqrt{s(\gamma+\mu) - 0.25(\gamma+\mu+qs)^2} \quad (2)$$

where μ is the birth/death rate, $q = (\gamma+\mu)/(\gamma+\mu+\nu)$, $s = (\nu+\mu)(R_0-1)$ and R_0 the basic reproductive number given by $R_0 = \beta/(\nu+\mu)$. We omit the subscript i for notational clarity. Although seasonality has not been shown to be important for syphilis[9], we note that for parameters consistent with syphilis natural history the period predicted by equation (2) does not change with the inclusion of seasonal forcing, which merely acts to ensure that the period is an integer number of years. The amplitude of oscillations is given by the variance in the number of infected individuals, which can be estimated through a diffusion approximation for reasonably large N as $\sigma_Y^2 = N(R_0-1)/R_0^2$ (ref. 29). These oscillations can also occur in the SIR model and persist in both models even when a significant fraction of individuals do not develop immunity (see Supplementary Fig. 1). As the metapopulation becomes increasingly coupled ($\varepsilon \to 1$), these oscillations become synchronized in phase and frequency, until in the fully coupled system synchronized oscillations occur with period approximated by equation (2) with a basic reproductive number given by $\bar{R}_0 + \sigma_{R_0}^2/\bar{R}_0$, where $\bar{R}_0$ is the mean and $\sigma_{R_0}^2$ the variance of the reproductive number for each population.

The model parameters γ, R_0 and N for New York City and Houston in Fig. 2b were estimated from the period, amplitude and mean of the oscillations in case reports, by making the simplifying assumption that the number of reported cases $C \approx fY\nu$, where f is the fraction of incident infections that are reported. For this illustration we assume that the other model parameters are fixed ($f = 0.5$, $\nu = 9$ in New York City and 6 in Houston, and $\mu = 0.03$).

The impact of different levels of coupling (ε) on cross-correlation of incidence (Fig. 3b, c) was examined numerically for a metapopulation where R_0 varies across cities according to a lognormal distribution (a few cities have high R_0), with mean 2 and variance 0.5 (although the results are closely consistent for different values of the variance, including zero). The distribution of N was assumed to follow a power law, in agreement with the decennial census estimates of the US city sizes in 1970 (ref. 30), but only a small fraction (1–5%) of the total population is assumed to be at risk of infection. The average cross-correlation $\bar{\rho}$ shown in Fig. 3c is for 5,000-yr simulations. All other model parameters are fixed ($\nu = 6$, $\mu = 0.03$, $\gamma = 0.05$).

Received 30 June; accepted 30 September 2004; doi:10.1038/nature03072.

1. Bjornstad, O. N. & Grenfell, B. T. Noisy clockwork: Time series analysis of population fluctuations in animals. *Science* **293,** 638–643 (2001).
2. Pascual, M., Rodo, X., Ellner, S. P., Colwell, R. & Bouma, M. J. Cholera dynamics and el Nino-Southern Oscillation. *Science* **289,** 1766–1769 (2000).
3. Nakashima, A. K., Rolfs, R. T., Flock, M. L., Kilmarx, P. & Greenspan, J. R. Epidemiology of syphilis in the United States, 1941–1993. *Sex. Transm. Dis.* **23,** 16–23 (1996).
4. Morgan, C. A., Lukehart, S. A. & Van Voorhis, W. C. Protection against syphilis correlates with specificity of antibodies to the variable regions of *Treponema pallidum* repeat protein K. *Infect. Immun.* **71,** 5605–5612 (2003).
5. Fox, K. K. *et al.* Longitudinal evaluation of serovar-specific immunity to *Neisseria gonorrhoeae*. *Am. J. Epidemiol.* **149,** 353–358 (1999).
6. Schmidt, K. A. *et al.* Experimental gonococcal urethritis and reinfection with homologous gonococci in male volunteers. *Sex. Transm. Dis.* **28,** 555–564 (2001).
7. Chatfield, C. *The Analysis of Time Series: an Introduction* 6th edn (Chapman & Hall/CRC, Boca Raton, 2003).
8. Grenfell, B. T., Bjornstad, O. N. & Kappey, J. Travelling waves and spatial hierarchies in measles epidemics. *Nature* **414,** 716–723 (2001).
9. Hethcote, H. W. & Yorke, J. A. *Gonorrhea Transmission Dynamics and Control in Lecture Notes Biomath* no. 56 (Springer, Berlin, 1984).
10. Garnett, G. P., Aral, S. O., Hoyle, D. V., Cates, W. & Anderson, R. M. The natural history of syphilis: Implications for the transmission dynamics and control of infection. *Sex. Transm. Dis.* **24,** 185–200 (1997).
11. Garnett, G. P., Mertz, K. J., Finelli, L., Levine, W. C. & St Louis, M. E. The transmission dynamics of gonorrhoea: modelling the reported behaviour of infected patients from Newark, New Jersey. *Phil. Trans. R. Soc. Lond. B* **354,** 787–797 (1999).
12. Hook, E. W. *et al.* Delayed presentation to clinics for sexually transmitted diseases by symptomatic patients—A potential contributor to continuing STD morbidity. *Sex. Transm. Dis.* **24,** 443–448 (1997).
13. Greenberg, J. B. *et al.* Learning from clients: An opportunity for sexually transmitted disease programs. *J. Public Health Manage Pract.* **8,** 59–68 (2002).
14. Wasserheit, J. N. & Aral, S. O. The dynamic topology of sexually transmitted disease epidemics: implications for prevention strategies. *J. Infect. Dis.* **174** (suppl. 2), S201–S213 (1996).
15. Hamers, F. F. *et al.* Syphilis and Gonorrhea in Miami—Similar clustering, different trends. *Am. J. Public Health* **85,** 1104–1108 (1995).
16. Bailey, N. T. J. *The Mathematical Theory of Infectious Diseases and its Applications* 2nd edn (Griffin, London, 1975).
17. Lloyd, A. L. & May, R. M. Spatial heterogeneity in epidemic models. *J. Theor. Biol.* **179,** 1–11 (1996).
18. U.S. Department of Transportation Bureau of Transportation Statistics. *National Transportation Statistics 2003* (U.S. Government Printing Office, Washington DC, 2003).
19. Cliff, A. D., Haggett, P. & Smallman-Raynor, M. in *Deciphering Global Epidemics: Analytical Approaches to the Disease Records of World Cities, 1888–1912* (eds Baker, A. R. H., Dennis, R. & Holdsworth, D.) (Cambridge Univ. Press, Cambridge, 1998).
20. Wallace, R., Huang, Y. S., Gould, P. & Wallace, D. The hierarchical diffusion of AIDS and violent crime among US metropolitan regions: Inner-city decay, stochastic resonance and reversal of the mortality transition. *Soc. Sci. Med.* **44,** 935–947 (1997).
21. Keeling, M. J. & Rohani, P. Estimating spatial coupling in epidemiological systems: a mechanistic approach. *Ecol. Lett.* **5,** 20–29 (2002).
22. Lloyd, A. L. & Jansen, V. A. A. Spatiotemporal dynamics of epidemics: synchrony in metapopulation models. *Math. Biosci.* **188,** 1–16 (2004).
23. Aral, S. O. The social context of syphilis persistence in the southeastern United States. *Sex. Transm. Dis.* **23,** 9–15 (1996).
24. Kuperman, M. & Abramson, G. Small world effect in an epidemiological model. *Phys. Rev. Lett.* **86,** 2909–2912 (2001).
25. Chesson, H. W., Dee, T. S. & Aral, S. O. AIDS mortality may have contributed to the decline in syphilis rates in the United States in the 1990s. *Sex. Transm. Dis.* **30,** 419–424 (2003).
26. Kahn, R. H., Heffelfinger, J. D. & Berman, S. M. Syphilis outbreaks among men who have sex with men—A public health trend of concern. *Sex. Transm. Dis.* **29,** 285–287 (2002).
27. Wolitski, R. J., Valdiserri, R. O., Denning, P. H. & Levine, W. C. Are we headed for a resurgence of the HIV epidemic among men who have sex with men? *Am. J. Public Health* **91,** 883–888 (2001).
28. Bjørnstad, O. N., Ims, R. A. & Lambin, X. Spatial population dynamics: analyzing patterns and processes of population synchrony. *Trends Ecol. Evol.* **14,** 427–432 (1999).
29. Nåsell, I. Stochastic models of some endemic infections. *Math. Biosci.* **179,** 1–19 (2002).
30. Gibson, C. *Population of the 100 Largest Cities and Other Urban Places in the United States: 1790–1990* (Working Paper No. 27, Population Division, US Census Bureau, Washington DC, 1998).

Supplementary Information accompanies the paper on **www.nature.com/nature**.

Acknowledgements The authors are grateful to M. Flock and S. Berman at the US Centers for Disease Control and Prevention for making available the disease case reports and for discussion on data quality. We also thank J. Truscott, J. Lewis, P. White, N. Ferguson, S. Riley and O. Bjørnstad for advice and help in analysis of periodic time-series data. N.C.G. and C.F. would like to thank the Royal Society, and G.P.G. and C.F. the Medical Research Council for funding.

Competing interests statement The authors declare that they have no competing financial interests.

Correspondence and requests for materials should be addressed to N.C.G. (n.grassly@imperial.ac.uk).

How the Venus flytrap snaps

Yoël Forterre[1], Jan M. Skotheim[2,4], Jacques Dumais[3] & L. Mahadevan[3,4]

[1]*IUSTI CNRS, Université de Provence, 5 rue Enrico Fermi, 13453 Marseille Cedex 13, France*
[2]*Department of Applied Mathematics and Theoretical Physics, Centre for Mathematical Sciences, University of Cambridge, Cambridge CB3 0WA, UK*
[3]*Department of Organismic and Evolutionary Biology, Harvard University Biological Laboratories, 16 Divinity Avenue, and*
[4]*Division of Engineering and Applied Sciences, Harvard University, Pierce Hall, 29 Oxford Street, Cambridge, Massachusetts 02138, USA*

The rapid closure of the Venus flytrap (*Dionaea muscipula*) leaf in about 100 ms is one of the fastest movements in the plant kingdom. This led Darwin to describe the plant as "one of the most wonderful in the world"[1]. The trap closure is initiated by the mechanical stimulation of trigger hairs. Previous studies[2–7] have focused on the biochemical response of the trigger hairs to stimuli and quantified the propagation of action potentials in the leaves. Here we complement these studies by considering the post-stimulation mechanical aspects of Venus flytrap closure. Using high-speed video imaging, non-invasive microscopy techniques and a simple theoretical model, we show that the fast closure of the trap results from a snap-buckling instability, the onset of which is controlled actively by the plant. Our study identifies an ingenious solution to scaling up movements in non-

muscular engines and provides a general framework for understanding nastic motion in plants.

Plants are not known for their ability to move quickly. Nevertheless, rapid plant movements are involved in essential functions such as seed and pollen dispersal (exploding fruits in Impatiens, squirting cucumber and trigger plants), defence (sensitive mimosa) and nutrition (Venus flytrap, *Aldrovanda vesiculosa*, bladderwort). Of these spectacular examples that have long fascinated scientists, the leaves of the Venus flytrap (Fig. 1a), which snap together in a fraction of second to capture insects, have long been a paradigm for study; however, the mechanism by which this engine works remains poorly understood[1,5,8–13]. The most frequently proposed explanations are an irreversible, acid-induced wall loosening[8], and a rapid loss of turgor pressure in 'motor cells'[13]. However, the validity of both mechanisms has recently been questioned[5,11] on the grounds that these cellular mechanisms alone cannot explain the rapidity of closure of the entire leaf on a macroscopic scale; this has led to the suggestion[5] that elastic deformations might be important.

Any mechanistic explanation requires an understanding of the geometry of snapping. Therefore, we first quantified the change in leaf geometry during closure by painting sub-millimetric ultraviolet-fluorescent dots on the external face of the leaves and filmed closure under ultraviolet light, using high speed video at 400 frames per second (Fig. 1b, see Supplementary Methods for a movie). Using a pair of mirrors to record stereo images, we reconstructed the leaf geometry and the change therein using triangulation (Fig. 1b, c; see Methods). As Darwin had already noted[1], the leaf is curved outward (convex) in the open state and curved inward (concave) in the closed state (Fig. 1a). The leaf shape can be naturally characterized in terms of its spatially averaged mean curvature (κ_m) and its spatially averaged gaussian curvature (κ_g), both of which are invariant under rigid body motions and are thus indicators of shape. In Fig. 1d we plot κ_m as a function of time and observe that the snapping motion is characterized by three phases: a slow initial phase (20% of total displacement in 1/3 s), a rapid intermediate phase (60% of total displacement in 1/10 s) and finally a second slow phase (20% of total displacement in 1/3 s). The existence of the three phases is consistently observed, but the quantitative values may vary. Most of the leaf displacement occurs in the intermediate phase, during which the leaf geometry changes from convex to concave. Figure 1e shows κ_g as a function of time. We see that κ_g is not constant, and also that κ_g changes slowly and then rapidly as it passes through a minimum. As changes in κ_g correspond to stretching the mid-plane of the leaf[14], these observations imply that closure is characterized by the slow storage of elastic energy followed by its rapid release.

To understand the origin of these curvature changes, we measured local strains by recording the position of fiducial markers over the entire outer surface of a leaf before and after closure (see Methods). Our measurements of the strain (Fig. 2a) are consistent with earlier point-wise measurements[5,12], but go beyond these by characterizing the spatial structure of the strain field over the entire leaf. Figure 2a shows that the maximum strain perpendicular to the midrib (*x*-direction) is six times the maximum strain parallel to

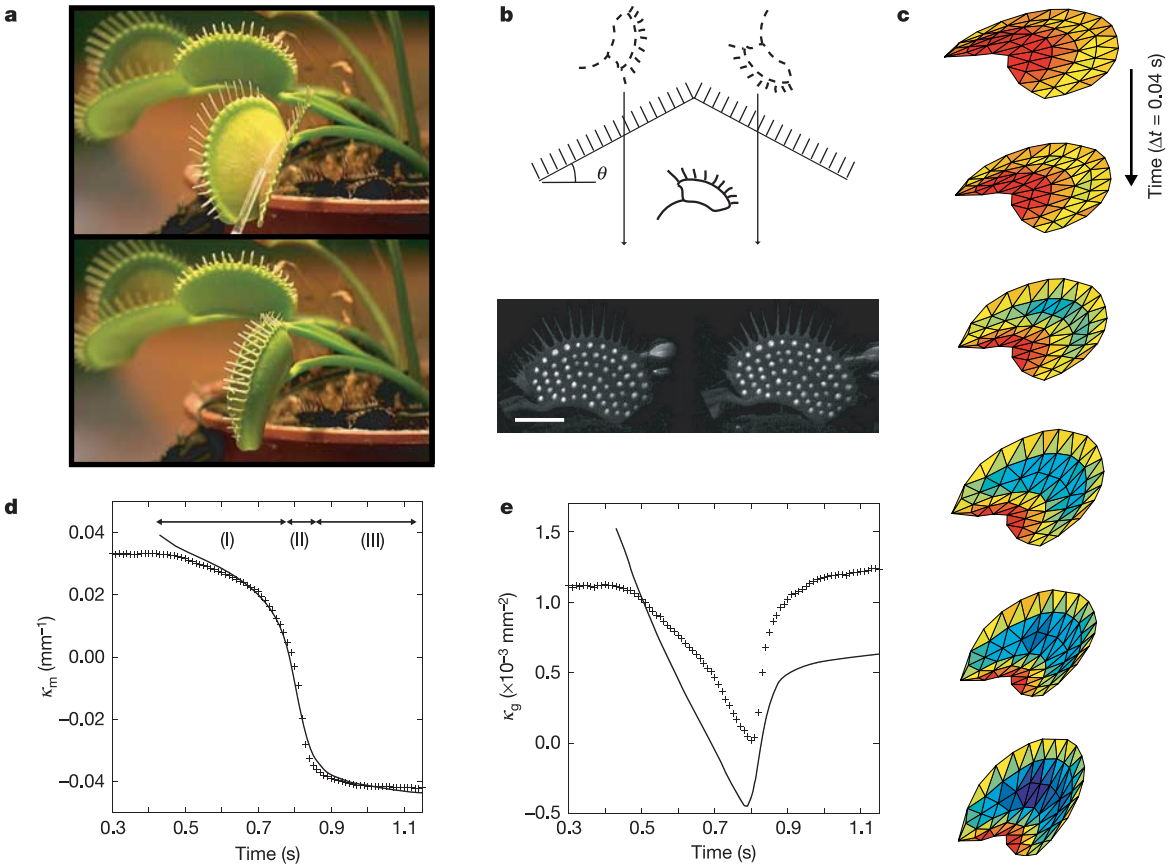

Figure 1 Dynamics of Venus flytrap closure. **a**, The Venus flytrap in its open and closed states. **b**, Schematic diagram of the imaging technique and typical stereo image showing fluorescent dots on the leaf surface under ultraviolet light. **c**, Dynamic sequence of the leaf closure. The time between images is 0.04 s. Colour indicates the value of the local mean curvature (blue $\kappa_m < 0$, red $\kappa_m > 0$). **d**, **e**, The spatially averaged mean curvature κ_m (**d**) and the spatially averaged gaussian curvature κ_g (**e**) as a function of time. The plant was triggered at $t = 0$. The closure dynamics are characterized by three phases (I–III): a slow initial phase, a rapid intermediate phase and finally a second slow phase. The solid line corresponds to the theoretical model (see Methods). Scale bar, 1 cm in (**a**) and (**b**).

the midrib (*y*-direction). Furthermore, we find that the strains on the inner surface of the leaf are ≤1%, implying that closure is triggered primarily by differential strains in the *x*-direction. To corroborate this picture, we cut recently-closed leaves to determine the residual strains in them. Cutting a closed leaf in the *x*-direction eliminates the constraining effect of curvature in the *y*-direction and allows it to recover its natural curvature in the *x*-direction, κ_{xn}, as seen in Fig. 2b. Similarly, cutting the leaf in the *y*-direction allows us to observe the natural curvature in the *y*-direction, κ_{yn}. We see that κ_{xn} reverses sign during closure, but κ_{yn} does not. This is consistent with previous observations[5] and provides quantitative evidence that a change in κ_{xn} drives leaf closure. Evidence supporting a mechanistic basis for this anisotropic deformation comes from microscopic examination of the leaf surface (see Supplementary Fig. 1); we observe that the cells on the outer surface are highly elongated in shape, with their long axis oriented along the *x*-axis. As the cylindrical cell wall is reinforced azimuthally by microfibrils[5], it follows that any changes in turgor would lead to deformations that are primarily in the *x*-direction, consistent with our macroscopic observations that κ_{xn} changes much more than κ_{yn}.

Although the molecular and cellular processes underlying the water movements that control anisotropic curvature changes remain poorly understood, we now argue that the macroscopic mechanism of closure is determined solely by leaf geometry. For a doubly-curved leaf (one that is curved in two orthogonal directions), bending and stretching modes of deformations are coupled[14], meaning that bending the leaf causes its mid-plane to be stretched. If the coupling is weak, the leaf can change its shape from open to closed by varying its gaussian curvature and stretch without a large energetic cost. In such a situation, the leaf deforms smoothly to accommodate the change in κ_{xn}. If the coupling is strong, the leaf will not deform much (owing to the large energetic cost of stretching its mid-plane), until eventually the change in κ_{xn} becomes so large that the leaf snaps shut rapidly (Fig. 3). To quantify the smooth–snapping transition, we modelled the leaf as a thin, weakly-curved elastic shell with principal natural curvatures κ_{xn} (which changes) and κ_{yn} (which remains constant) and initial curvatures $\kappa_x(t=0) = \kappa_y(t=0) = \kappa$ (see Methods). The shape of

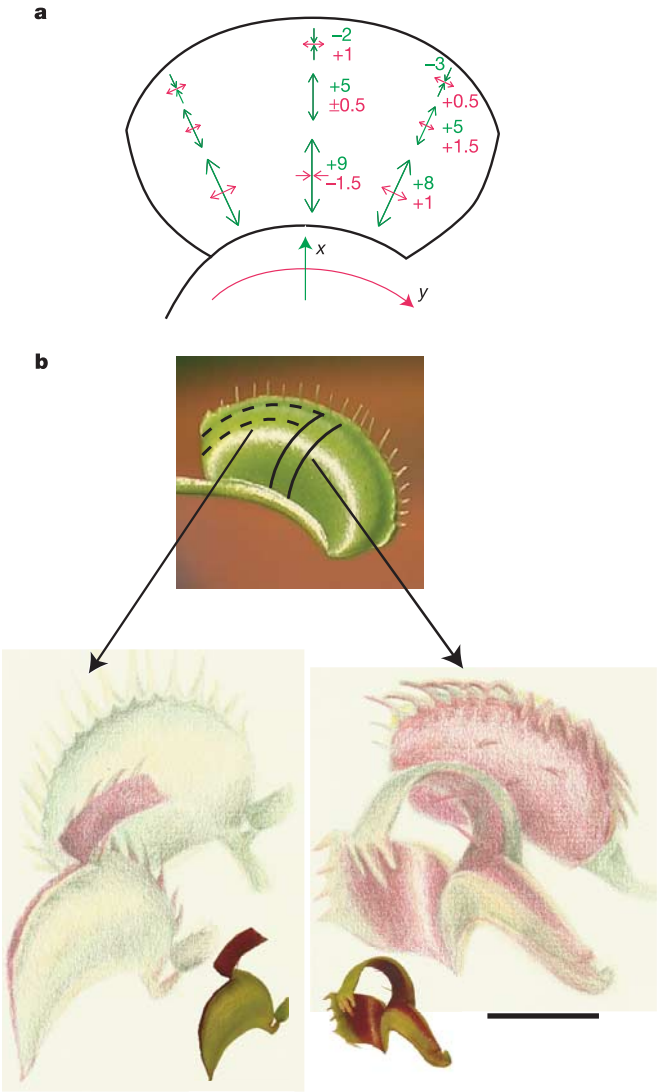

Figure 2 Strain field and natural curvature. **a**, Measured strain field of the outer face due to closure, where positive strains correspond to extension and negative strains correspond to contraction of the surface in the principal directions as shown. The maximum strain of 9% is perpendicular to the midrib (*x*-direction), whereas the strain parallel to the midrib (*y*-direction) is much smaller (±2%). **b**, Cutting the closed leaf along the dotted lines eliminates the coupling between bending and stretching in the doubly-curved leaf and shows κ_{xn} and κ_{yn}, the natural curvatures in the respective *x*- and *y*-directions. We find that κ_{yn} remains unchanged during leaf closure, but κ_{xn} changes actively and provides the motive force for snapping. The illustrations show the cut leaf overlaid on the uncut leaf; the smaller images show the cut leaf. For this leaf, the inner surface is red and the outer surface is green. Scale bar is for the illustration, 1 cm.

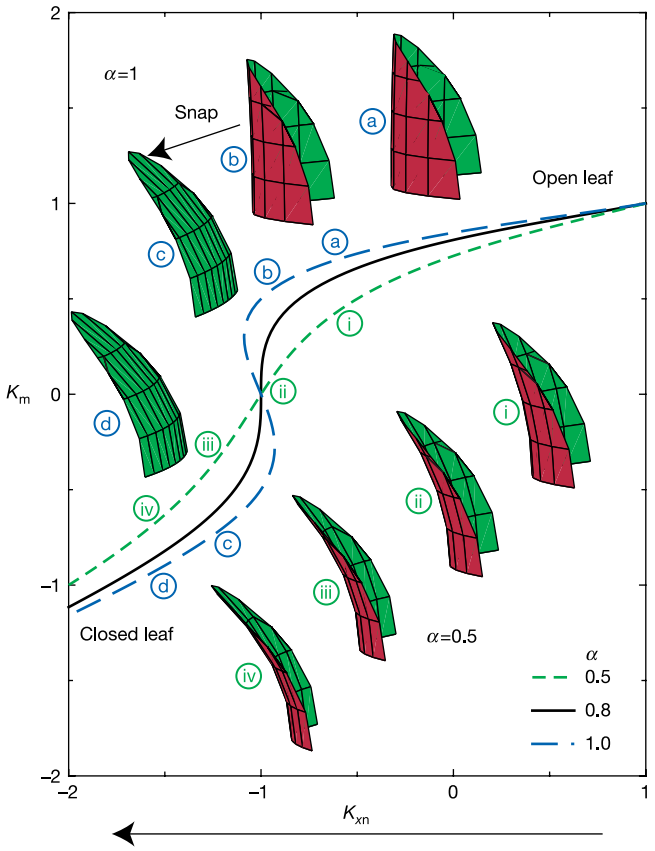

Figure 3 Smooth–snapping transition in leaf closure. We plot the dimensionless mean curvature $K_m = (K_x + K_y)/2$ as a function of the control parameter K_{xn} (see Methods). For $\alpha < \alpha_c = 0.8$ we observe a smooth transition from the open to the closed state, but for $\alpha > \alpha_c$ the system passes through a region of bistability before undergoing a rapid, 'snapping' transition. In the lower part of the figure we provide a schematic of the continuous transition ($\alpha = 0.5$); the upper part of the figure shows a similar schematic for the 'snapping' transition ($\alpha = 1$). Red denotes the inner surface and green denotes the outer surface of the leaf.

the leaf is found by minimizing the dimensionless elastic energy $U(\kappa_x, \kappa_y; \kappa_{xn}, \alpha) = U_{\text{bending}} + \alpha U_{\text{stretching}}$, which depends on the dimensionless natural curvature in the x-direction (K_{xn}, which is controlled by the plant), and also depends on the dimensionless geometric parameter $\alpha = L^4\kappa^2/h^2$, which quantifies the coupling between bending and stretching deformations in terms of the leaf thickness h, the leaf size L, and the observed curvature of the open leaf κ (see Methods). A larger value of α implies that it is relatively more difficult to stretch the mid-plane by changing the gaussian curvature of the leaf. In Fig. 3 we see that $U(\kappa_x, \kappa_y; \kappa_{xn}, \alpha)$ has a single minimum when $\alpha \leq \alpha_c$ (weak bending–stretching coupling), but has two minima when $\alpha > \alpha_c$ (strong bending–stretching coupling) for some values of K_{xn}. Our model thus predicts a region of bistability in which both the open and the closed states of the leaf are stable to small perturbations.

Consistent with this prediction, we have observed leaves that begin to close when stimulated, but do not snap or reach the closed state. However, by squeezing the leaves with our fingers we were able to induce a snap transition mechanically, indicating that the leaf was indeed in a bistable configuration. Because the amount of mid-plane stretching required for the leaf to close increases with α, the mechanical barrier to snapping is determined by this geometrical parameter. Thus we expect that large, highly curved leaves will release more energy and snap more rapidly than smaller, weakly curved leaves. To test this, we measured the speed of leaf closure as a function of the geometrical parameter α for many different leaves and plants. Figure 4a shows a clear positive correlation between the maximum speed of the snap and α. Interestingly, the time delay between the beginning of the motion and the snap increases with the parameter α (Fig. 4b), as does the maximum speed of snapping. This is probably because the delay reflects the time required to cross the stretching barrier, which increases with α. For a typical leaf $\alpha = L^4\kappa^2/h^2 \approx (1\,\text{cm})^4(0.1\,\text{cm}^{-1})^2/(0.1\,\text{cm})^2 \approx 1 \approx \alpha_c$, suggesting that the leaves are poised at the transition between smooth closing and snapping. As the plant is clearly best served both by minimizing the delay between triggering and closure, and snapping rapidly rather than closing smoothly, this value of α might not be a coincidence.

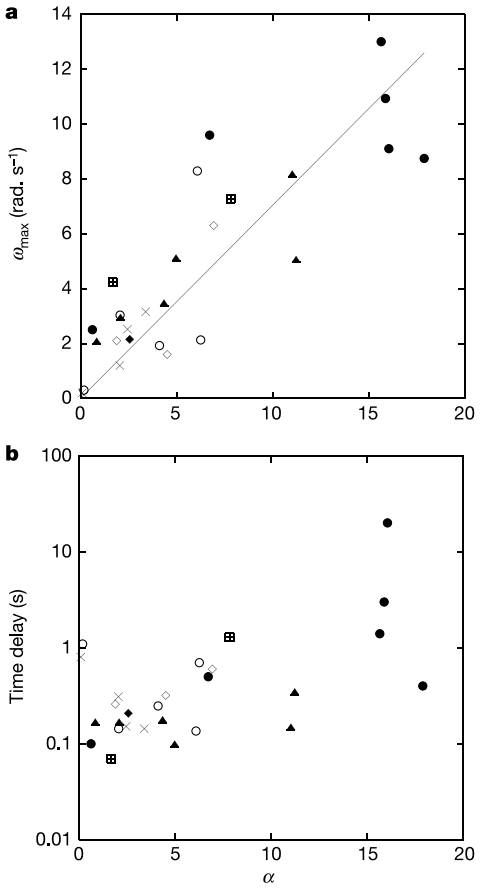

Figure 4 Speed of closure and delay between triggering and snapping. **a**, Maximum angular velocity ω plotted against α. **b**, The time between triggering the leaf and snapping, rapid closure plotted against α (note the semi-logarithmic scale). Identical symbols correspond to different leaves on the same plant.

The actual speed of snapping (the leaf closure time) is a critical parameter for trap function. Observations show that the motion is rapidly damped once the trap is closed. As the timescale of the fundamental bending mode of the leaf $\tau_B \approx (L^2h^{-1})(\rho/E)^{1/2} \approx 0.001$–$0.01$ s is much less than the observed timescale of the motion ($\sim$0.1–1 s), and we observe no ringing, we conclude that inertial effects are not relevant in setting the timescale of motion. Furthermore, on comparing the elastic force acting on the leaf, F_E, to the force due to motion through the external air, F_A, we see that $F_A/F_E \approx \rho_f V^2 L^2/Eh^3\kappa \approx 10^{-6}$, where $V = 1\,\text{cm}\,\text{s}^{-1}$ and ρ_f is the density of air. Hence the damping must occur internally. Because the leaf is highly hydrated, a natural candidate for damping is provided by the flow of interstitial water through the surrounding elastic tissue. The curvature change during closure induces a transient flow perpendicular to the leaf surface, which occurs over a timescale $\tau_P \approx \mu h^2/kE$ (refs 15, 16), where k is the hydraulic permeability of the leaf tissue, μ is the interstitial fluid viscosity and E is the drained bulk modulus of the tissue. Using a measured value of Young's modulus $E \approx 10\,\text{M Pa}$ and taking $k/\mu \approx 10^{-12}\,\text{m}^2\,\text{Pa}^{-1}\,\text{s}^{-1}$) (ref. 17) we find that $\tau_P \approx 0.1$ s, consistent with the snapping time. Our experiments on the response of the leaf tissue to impulsive and step loads are consistent with these estimates (see Supplementary Methods). A quantitative model that balances the change in elastic energy with the energy dissipated by fluid flow captures the three phases of snapping (Fig. 1d, e; see Methods and Supplementary Methods).

Our kinematic and mechanical measurements allow us to identify two distinct pieces in the puzzle of trap snapping: an active biochemical component and a passive elastic component. Upon stimulation, the plant 'actively' changes one of its principal natural curvatures, κ_{xn}, the microscopic mechanism for which remains poorly understood. Once this change occurs, the geometry of the doubly-curved leaf provides the mechanism by which elastic energy is both stored and released, and the hydrated nature of the leaf induces the rapid damping that is equally crucial for efficient prey capture. A single geometrical parameter (α) determines the nature of closure: if $\alpha \leq \alpha_c \approx 0.8$, the leaf closes smoothly, and if $\alpha > \alpha_c$, the leaf snaps rapidly. This ingenious solution to the problem of scaling up movements and speed from the cellular to the organ level in plants, nature's consummate hydraulic engineers, shows how controlling elastic instabilities in geometrically slender objects provides an alternative to the more common muscle-powered movements in animals. □

Methods

Stereoscopic reconstruction and curvature measurements

Plants were grown at room temperature (25 °C) and received 12 h of fluorescent light daily. All experiments were performed on healthy adult specimens. To record the three-dimensional (3D) shape of the leaf during closure, freshly excised traps were positioned in front of a pair of mirrors 2 m from a high-speed camera (Phantom V; Fig. 1b). Excised traps behaved as uncut traps as long as the time between excision and triggering was less than a few minutes. The stereo videos were post-processed using ImageJ software (http://rsb.info.nih.gov/ij/) to give the coordinates of the fluorescent dots for both left and right images. The corresponding 3D coordinates were obtained using a far field triangulation scheme (see Supplementary Methods for details).

We used two different approaches to compute local curvatures on the reconstructed leaf surface: first, global interpolation of the surface using p-splines (Matlab software) with the curvatures computed using finite differences, and second, local quadratic approximation of the surface[18]. Although the two methods gave similar qualitative

outcomes, quantitative differences between the two results (~30%) arose due to intrinsic noise in the reconstruction and the limited number (~50) of points per leaf.

Strain field measurements

Moulds of the outer and inner surfaces of six different leaves were made before and after closure using a non-invasive replica technique[19]. We used a high-resolution digital camera fitted with a microscope lens to track the microscopic hairs of the outer face and the digestive glands of the inner face. The local strain field associated with closure (that is, the principal strains and the corresponding principal directions) was computed by local orientation-averaging of the strains (see Supplementary Methods) before determining their maxima and minima.

Measurement of α, maximum angular velocity and time delay

$\alpha = L^4\kappa^2/h^2$ was computed experimentally using $L = (L_1 + L_2)/4$, where L_1 is the length across the leaf measured parallel to the midrib and L_2 is the length measured perpendicular to the midrib. Measuring L/h for over 30 traps, we find that $L/h \approx 20$. κ is the initial mean curvature of the leaf. The maximum speed of the snap is the maximum angular speed of the vector perpendicular to the midrib that extends to the centre of the leaf's edge. The time delay is the time it takes the mean curvature to change from 5% to 50% of the total mean curvature change.

Elastic shell statics

We modelled the leaf as a thin, shallow shell with radius L, uniform thickness h, Young's modulus E, and natural curvatures κ_{xn}, κ_{yn}. Here we outline a minimal theory that captures the essential feature of these complex theories, namely that bending a doubly-curved shell leads to stretching because of changes in the gaussian curvature. This bend–stretch coupling is formalized in equations that describe the finite deformations of plates and shallow shells[20]. Postponing the consideration of a complete theory, here we opt for a simplified energetic treatment that neglects the role of Poisson contraction and extension to enable us to focus on the essential mechanisms involved. Experimental data shows us that we may approximate the leaf shape as an elliptic (or hyperbolic if the two principal curvatures have opposite sign) paraboloid given by $f = (\kappa_x x^2/2) + (\kappa_y y^2/2)$, where κ_x and κ_y are the spatially homogeneous principal curvatures. Consistent with our experimental observations, we take the natural curvature in the y-direction to be a constant, equal to the initial curvature in the x- and y-directions before snapping, so that $\kappa_x(t=0) = \kappa_y(t=0) = \kappa_{yn}(t) = \kappa$. Then we can write the dimensionless total energy due to bending and stretching[20]:

$$U(K_x, K_y; K_{xn}, \alpha) = U_{\text{bending}} + \alpha U_{\text{stretching}} = (K_x - K_{xn})^2 + (K_y - 1)^2 + \alpha(K_x K_y - 1)^2$$

where $K_x = \kappa_x/\kappa$, $K_y = \kappa_y/\kappa$ and $K_{xn} = \kappa_{xn}/\kappa$ are dimensionless. The geometric coupling parameter $\alpha = L^4\kappa^2/h^2$ characterizes the relative energy penalty of bending-to-stretching deformations. Minimizing $U(K_x,K_y;K_{xn},\alpha)$ with respect to K_x, K_y; that is, solving:

$$\frac{\partial U}{\partial K_x} = \frac{\partial U}{\partial K_y} = 0$$

for different values of α yields the change in leaf shape as a function of K_{xn}. When $\alpha > \alpha_c \approx 0.8$, there is just a single minimum, whereas for a typical leaf when $\alpha \approx 1$, we see the appearance of a second minimum (Fig. 3).

Poroelastic shell dynamics

To model the dynamics of snapping, we treat the leaf tissue as a poroelastic material. When the leaf snaps shut, the changes in curvature cause the movement of interstitial water relative to the elastic tissue, which dissipates energy. For an impermeable poroelastic plate with dimensionless curvatures $K_x(t)$ and $K_y(t)$ and fluid volume fraction ψ (ref. 16), balancing the elastic power due to curvature changes with the viscous dissipation rate due to fluid flow yields the dimensionless energy-balance equation (see Supplementary Methods):

$$\frac{\mathrm{d}U}{\mathrm{d}T} = A\left(\frac{\partial K_x(T)}{\partial T} + \frac{\partial K_y(T)}{\partial T}\right)\int_0^T e^{-(T-T')}\left[\frac{\partial K_x(T')}{\partial T'} + \frac{\partial K_y(T')}{\partial T'}\right]\mathrm{d}T'$$

where $A = 196/\pi^4$. Here we have used a scaled time $T = t/\tau_p$, where $\tau_p = (\psi\mu h^2)/(\pi^2 kE)$ is the poroelastic time, and have scaled the curvatures and elastic energy (U) as in the previous section. We assume that K_x and K_y follow the path of steepest descent in the energy potential. In the absence of microscopic physiological information for the change in dimensionless natural curvature upon x-direction changes, we chose the form $K_{xn} = 1 - \alpha(1 - e^{-bT})$. To fit the data in Fig. 1d, e we used $a = 3$, $b = 0.05$, $\tau_P = 1/94$ s and $\alpha = 1$. Other functional forms (for example, $K_{xn} = 1 - \alpha T$) do not change the qualitative dynamics of snapping, although quantitative aspects of the waiting time before the snap and the post-snap dynamics are affected.

Received 20 June; accepted 12 November 2004; doi:10.1038/nature03185.

1. Darwin, C. *Insectivorous Plants* (Murray, London, 1875).
2. Burdon-Sanderson, J. On the electromotive properties of the leaf of *dionaea* in the excited and unexcited states. *Phil. Trans. R. Soc. Lond.* **173,** 1–55 (1882).
3. Stuhlman, O. Jr & Darder, E. B. The action potentials obtained from Venus's-flytrap. *Science* **111,** 491–492 (1950).
4. Hodick, D. & Sievers, A. The action potential of *Dionaea muscipula* Ellis. *Planta* **174,** 8–18 (1988).
5. Hodick, D. & Sievers, A. On the mechanism of trap closure of Venus flytrap (*Dionaea muscipula* Ellis). *Planta* **179,** 32–42 (1989).
6. Sibaoka, T. Physiology of rapid movements in higher plants. *Annu. Rev. Plant Physiol.* **20,** 165–184 (1969).
7. Juniper, B. E., Robins, R. J. & Joel, D. M. *The Carnivorous Plants* (Academic, London, 1989).
8. Williams, S. E. & Bennet, A. B. Leaf closure in the Venus flytrap: an acid growth response. *Science* **218,** 1120–1122 (1982).
9. Stuhlman, O. A physical analysis of the opening and closing movements of the lobes of Venus' flytrap. *Bull. Torrey Bot. Club* **7,** 22–44 (1948).
10. Ashida, J. Studies on leaf movement of *Aldrovanda vesiculosa*. *Mem. Coll. Sci. Kyoto Imp. Univ., Ser. B* **9,** 141–244 (1934).
11. Morillon, R., Liénard, D., Chrispeels, M. J. & Lassalles, J.-P. Rapid movements of plants organs require solute-water cotransporters or contractile proteins. *Plant Physiol.* **127,** 720–723 (2001).
12. Brown, W. H. The mechanism of movement and duration of the effect of stimulation in the leaves of dionaea. *Am. J. Bot.* **3,** 68–90 (1916).
13. Hill, B. S. & Findlay, G. P. The power of movement in plants: the role of osmotic machines. *Q. Rev. Biophys.* **14,** 173–222 (1981).
14. Love, A. E. H. *A Treatise on the Mathematical Theory of Elasticity* 4th edn (Dover, New York, 1944).
15. Biot, M. A. General theory of three-dimensional consolidation. *J. Appl. Phys.* **12,** 155–165 (1941).
16. Skotheim, J. M. & Mahadevan, L. Dynamics of poroelastic filaments. *Proc. R. Soc. Lond. A* **460,** 1995–2020 (2004).
17. Frensch, J. & Steudle, E. Axial and radial hydraulic resistance to roots of maize (*Zea mays L.*). *Plant Physiol.* **91,** 719–726 (1989).
18. Dumais, J. & Kwiatkowska, D. Analysis of surface growth in shoot apices. *Plant J.* **31,** 229–241 (2002).
19. Green, P. B., Havelange, A. & Bernier, G. Floral morphogenesis in Anagallis: Scanning-electron-micrograph sequences from individual growing meristems before, during, and after the transition to flowering. *Planta* **185,** 502–512 (1991).
20. Mansfield, E. H. *The Bending and Stretching of Plates* 2nd edn (Cambridge Univ. Press, Cambridge, 1989).

Supplementary Information accompanies the paper on **www.nature.com/nature**.

Acknowledgements We thank F. Shindler for the illustrations in Fig. 2. We acknowledge support via the Norwegian Research Council (J.M.S.) and the Schlumberger Chair Fund (L.M.) at Cambridge University, where this work was begun and primarily done.

Competing interests statement The authors declare that they have no competing financial interests.

Correspondence and requests for materials should be addressed to L.M. (lm@deas.harvard.edu).

Simulation and validation of modelled sphingolipid metabolism in *Saccharomyces cerevisiae*

Fernando Alvarez-Vasquez[1,2], Kellie J. Sims[1,2], L. Ashley Cowart[1], Yasuo Okamoto[1], Eberhard O. Voit[1,2,3] & Yusuf A. Hannun[1]

[1]*Department of Biochemistry and Molecular Biology and* [2]*Department of Biostatistics, Bioinformatics, and Epidemiology, Medical University of South Carolina, Charleston, South Carolina 29425, USA*
[3]*The Wallace H. Coulter Department of Biomedical Engineering, Georgia Institute of Technology and Emory Medical School, 313 Ferst Drive, Atlanta, Georgia 30332-0535, USA*

Mathematical models have become a necessary tool for organizing the rapidly increasing amounts of large-scale data on biochemical pathways and for advanced evaluation of their structure and regulation. Most of these models have addressed specific pathways using either stoichiometric[1] or flux-balance analysis[2], or fully kinetic Michaelis–Menten representations[3], metabolic control analysis[4], or biochemical systems theory[5–7]. So far, the predictions of kinetic models have rarely been tested using direct experimentation. Here, we validate experimentally a biochemical systems theoretical model of sphingolipid metabolism in yeast[8]. Simulations of metabolic fluxes, enzyme deletion and the effects of inositol (a key regulator of phospholipid metabolism) led to predictions that show significant concordance with experimental results generated post hoc. The model also allowed the simulation of the effects of acute perturbations in fatty-acid precursors of sphingolipids, a situation that is not amenable to direct experimentation. The results demonstrate that modelling now allows testable predictions as well as the design and evaluation

Supplementary Information for "How the Venus flytrap snaps"

Plant material

Plants were provided by the nurseries *Nature et Paysage* (French National Collection, 32360 Peyrusse-Massas, France), and *South West Carnivorous Plants* (2 Rose Cottages, Cullompton, EX15 3JJ, United Kingdom).

Stereoscopic reconstruction and curvatures measurements

To record the 3D shape of the leaf during closure, freshly excised traps were positioned in front of a pair of mirrors two meters from a high-speed camera (Phantom V; Fig. 1b). Excised traps behaved as uncut traps as long as the time between excision and triggering was less than a few minutes. The stereo videos were post-processed (ImageJ software, http://rsb.info.nih.gov/ij/) to give the coordinates of the fluorescent dots for both left and right images. The corresponding 3D coordinates (x,y,z) were obtained using a far field triangulation scheme: $x = (x_r + x_l)/(2\cos(2\theta))$; $y = (y_r + y_l)/2$; $z = (x_r - x_l)/(2\sin(2\theta))$, where θ is defined in Fig. 1b. As discussed in Methods, we used both a local (quadratic surface) and a global (spline) approach to determine the leaf curvatures.

Strain field measurements

Moulds of the outer and inner surface of six different leaves were made before and after closure using a non-invasive replica technique[20]. To avoid any bias due to the 3D shape of the leaf, a 2D impression of the replica was made by applying a thin (typically 0.1 mm) transparent film of nail polish onto the mould. The film was peeled off before it completely dried and placed between two microscope cover slips. We used a high-resolution digital camera fitted with a microscope lens to track the relative movement of microscopic hairs on the outer face and the digestive

glands on the inner face. The leaf was divided into 2mm x2mm windows each containing typically 50 of these fiducial markers. For each window, the position of each marker *i* before closure, $(x_1,y_1)_i$ and after closure, $(x_2,y_2)_i$ was obtained. The local strain $(\Delta l/l)(\phi)$ in a given direction ϕ was computed using the formula $\frac{\Delta l}{l}(\phi) = \frac{1}{N_\phi}\sum_{ij}\frac{\sqrt{(x_{2i}-x_{2j})^2+(y_{2i}-y_{2j})^2}-\sqrt{(x_{1i}-x_{1j})^2+(y_{1i}-y_{1j})^2}}{\sqrt{(x_{1i}-x_{1j})^2+(y_{1i}-y_{1j})^2}}$, where the sum is over all pairs (i,j) for which the position vector was in the window $[\phi, \phi+d\phi]$ and N_ϕ is the number of such pairs. Assuming that the strain field is homogeneous in the selected window, it can been shown easily that $\frac{\Delta l}{l}(\phi) = \lambda_1\cos(\phi-\phi_0)+\lambda_2\sin(\phi-\phi_0)$, where λ_1, λ_2 are the principal values of the strain field and ϕ_0 is the angle of the principal axes with respect to the coordinate reference frame (Supplementary Fig. 1). We observe that the principal directions and the maximum strains are strongly correlated with the highly anisotropic cell shapes on the outer surface of the leaf.

Temporal response of the leaf tissue to impulsive and step loads

To corroborate our simple estimates for the dynamical time scales based on the geometry, elasticity and hydraulic permeability of the leaf, we directly measured the response time of the tissue to both impulsive and step loads. A thin strip of a closed leaf was clamped at one end and free at the other. If an impulsive load is applied at the free end, then we see a short ringing transient of period ~ 10 ms (Supplementary Fig. 1a), consistent with our estimate for the inertial (bending) mode which is much faster than the time of closure. If on the other hand the strip is released suddenly after being statically deflected at the other end for a while, we get a very different response. In Supplementary Fig. 1b, we see that after a short inertial transient the unloading is best described by a single exponential with a time constant $\tau_p \sim$ 0.1-0.4 s, consistent with our simple poroelastic picture as the dominant mechanism operating during the dynamics of snapping.

Poroelastic shell model: dynamics

When the leaf snaps shut, the stored elastic energy is dissipated via the viscous flow within the leaf tissue. To model the dynamics of snapping we treat the leaf tissue as a poroelastic material: a linearly elastic solid skeleton with an interstitial fluid (i.e. a wet sponge). Following Skotheim and Mahadevan[16], we see that an impermeable poroelastic plate with curvatures κ_x (t) and κ_y (t), Young's modulus E, Poisson's ratio $\nu = 0$ for the elastic skeleton, and fluid volume fraction Ψ, generates a pressure in the interstitial fluid in response to mid-plane mean curvature given by $p = \frac{4}{\pi^2 \psi} h\, \kappa\, E\, Sin\left(\frac{\pi z}{h}\right) \int_0^t e^{-\frac{(t-t')}{\tau_p}} \left[\frac{\partial \kappa_x(t')}{\partial t'} + \frac{\partial \kappa_y(t')}{\partial t'}\right] dt'$, where the poroelastic time scale is $\tau_p = \frac{\psi^2 \mu h^2}{\pi^2 k E}$. This expression arises from the solution of a Darcy-type diffusion equation for the fluid pressure, which in turn gives rise to a moment resisting the bending $M_f = \psi \int_{-h/2}^{h/2} p\, z\, dz$ where z is the coordinate perpendicular to the leaf surface. Fluid motion through the tissue leads to dissipation with a rate $P_d = \int M_f \left(\frac{\partial \kappa_x}{\partial t} + \frac{\partial \kappa_y}{\partial t}\right) dA$. Then, balancing the elastic power with the viscous dissipation rate yields the dimensionless equation stated in the Methods section $\frac{dU}{dT} = A \left(\frac{\partial K_x(T)}{\partial T} + \frac{\partial K_y(T)}{\partial T}\right) \int_0^T e^{-(T-T')} \left[\frac{\partial K_x(T')}{\partial T'} + \frac{\partial K_y(T')}{\partial T'}\right] dT'$, where $A = \frac{196}{\pi^4}$. Here the time is scaled with the poroelastic time $t = \tau_p\, T$, curvatures are scaled with the initial curvature $\kappa_x = \kappa\, K_x$, $\kappa_y = \kappa\, K_y$, and the elastic energy is scaled with the bending energy, $u = C\, E\, h^3\, \kappa^2\, U$, where the dimensionless energy U is given in the Methods section

Definition of variables used in the text

κ_x = observed curvature in the direction perpendicular to the midrib (x-direction).

κ_y = observed curvature in the direction parallel to the midrib (y-direction).

κ_{xn} = natural curvature in the x-direction.

$\kappa_{yn} = \kappa =$ natural curvature in the *y*-direction.

$\kappa_{x0} = \kappa =$ initial curvature in the *x*-direction.

$\kappa_{y0} = \kappa =$ initial curvature in the *y*-direction.

$\kappa_g = \kappa_x \kappa_y =$ Gaussian curvature.

$\kappa_m = \dfrac{\kappa_x + \kappa_y}{2} =$ mean curvature.

capitalized symbols, e.g. K_{xn} refer to the scaled (dimensionless) versions of the same quantities, i.e. $K_{xn} = \dfrac{\kappa_{xn}}{\kappa}$ etc.

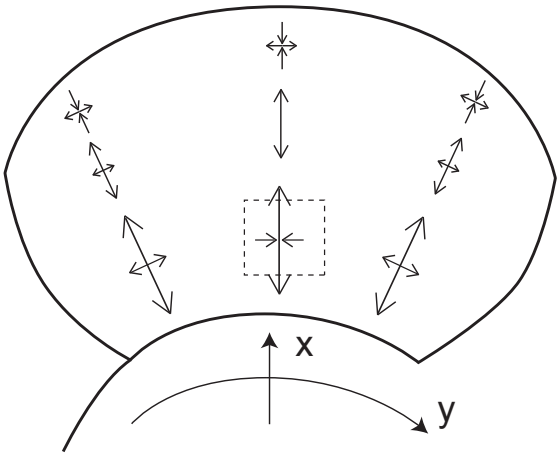

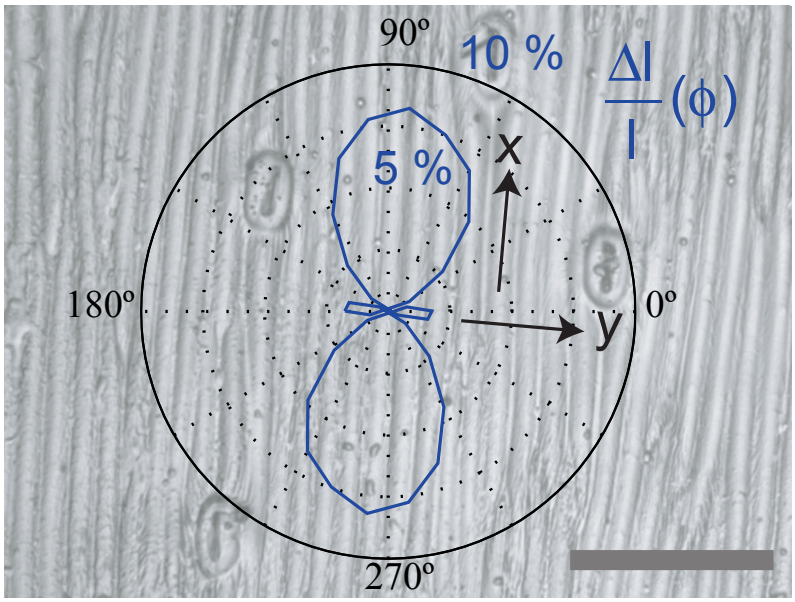

Supplementary Figure 1a Typical measurements of the local strain field associated with leaf closure, determined using the replica technique. The arrows indicate the sign of the strain and the size of the lines indicate their magnitude. **b** The local strains $(\Delta l/l)(\phi)$ measured on the outer surface of the leaf inside the dashed region corresponding to a region close to the midrib aqre superposed on a micrograph of the leaf surface. We note that the principal strains and directions are strongly correlated with the cell orientations. Since the cells are reinforced azimuthally by microfibrils, but are soft axially, the strain field is consistent with the constraints imposed by the microstructure of the leaf surface; thus closure occurs primarily because of changes in the natural curvature in the *x*-direction κ_{xn}. Scale bar: 100 μm.

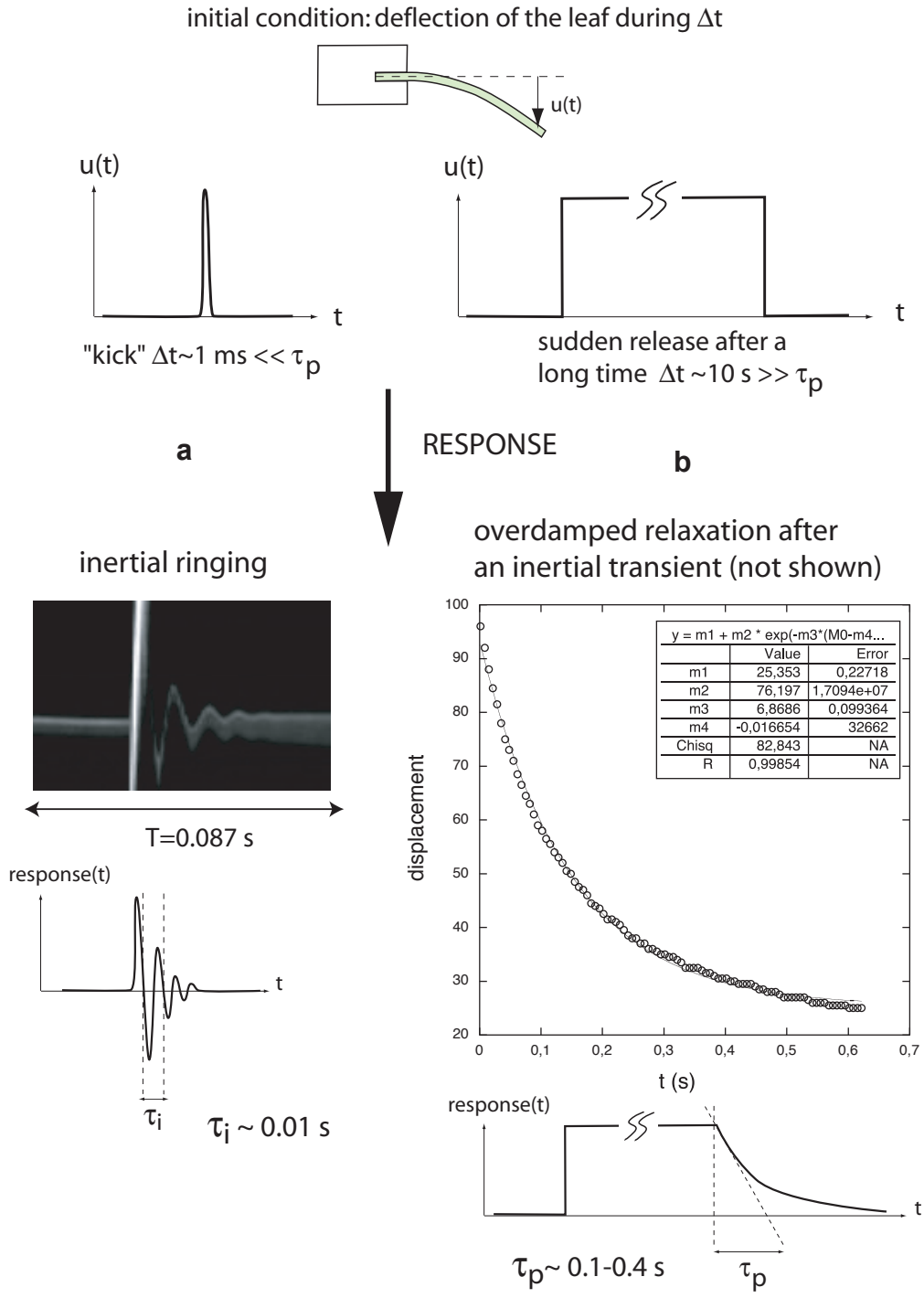

Supplementary Figure 2 The response of a strip of the closed leaf to impulse and step loads, when one end is clamped and the other end subject to a displacement *u(t).*
a, shows the response to an impulsive load that acts over a time of ~1 ms, leading to an inertial ringing that is purely elastic and corresponds to a time scale of ~0.01 s, which is much faster than the observed speed of closure. **b**, shows the response to the unloading of a step displacement that is applied on a longer time scale giving the leaf time to equilibrate, before being released suddenly. In this case, we see that, after a short inertial transient (not shown), the behavior of the leaf is well fit by a single exponential with a time constant τ_p~0.1-0.4 s, consistent with a poroelastic mechanism for the overdamped dynamics of the snapping.